Pure Appl. Geophys. 175 (2018), 685–705

https://doi.org/10.1007/s00024-017-1659-y

Pure and Applied Geophysics

Probabilistic Seismic Hazard Assessment for Himalayan–Tibetan Region from Historical and Instrumental Earthquake Catalogs

M. Moklesur Rahman,[1,2,3] Ling Bai,[1] Nangyal Ghani Khan,[1] and Guohui Li[1]

Abstract—The Himalayan–Tibetan region has a long history of devastating earthquakes with wide-spread casualties and socio-economic damages. Here, we conduct the probabilistic seismic hazard analysis by incorporating the incomplete historical earthquake records along with the instrumental earthquake catalogs for the Himalayan–Tibetan region. Historical earthquake records back to more than 1000 years ago and an updated, homogenized and declustered instrumental earthquake catalog since 1906 are utilized. The essential seismicity parameters, namely, the mean seismicity rate γ, the Gutenberg–Richter b value, and the maximum expected magnitude M_{max} are estimated using the maximum likelihood algorithm assuming the incompleteness of the catalog. To compute the hazard value, three seismogenic source models (smoothed gridded, linear, and areal sources) and two sets of ground motion prediction equations are combined by means of a logic tree on accounting the epistemic uncertainties. The peak ground acceleration (PGA) and spectral acceleration (SA) at 0.2 and 1.0 s are predicted for 2 and 10% probabilities of exceedance over 50 years assuming bedrock condition. The resulting PGA and SA maps show a significant spatio-temporal variation in the hazard values. In general, hazard value is found to be much higher than the previous studies for regions, where great earthquakes have actually occurred. The use of the historical and instrumental earthquake catalogs in combination of multiple seismogenic source models provides better seismic hazard constraints for the Himalayan–Tibetan region.

Key words: Himalayan–Tibetan region, probabilistic seismic hazard, peak ground acceleration, Gutenberg–Richter b value, logic tree.

1. Introduction

The Himalayan–Tibetan region has long been regarded as one of the world's biggest and highest seismotectonic active regimes resulting from ongoing collision between the Indian and Eurasian plates since Tertiary period (Avouac and Tapponnier 1993; Bai et al. 2017; Tapponnier et al. 2001; Zhao et al. 2012). This region encompasses the intra-continental active crustal Tibetan plateau in the center, the Himalaya orogen in the south, Pamir–Hindu Kush deep subduction zone in the west, and Tien Shan mountain belt in the north. Historical documents (Table 1) state that this region has produced many catastrophic earthquakes. The most recent damaging earthquake affecting central Himalaya is the 25 April 2015, M_w 7.8 Gorkha, Nepal earthquake which caused nearly 9000 casualties, destroyed over fifty thousands of buildings, and gave rise to huge economic losses (Bilham 2015). In the current century, the largest earthquake affecting the China mainland, the eastern margin of Tibetan plateau in particular, was the 12 May 2008, M_w 7.9 Wenchuan earthquake. It was occurred in Sichuan region resulting more than 80,000 human lives losses with ~U.S. $110 billion damage (Wang et al. 2012). Thus, the entire Himalayan–Tibetan region is facing a significant seismic hazard and consequent seismic risk.

Since the pioneer work by Cornell (1968), the probabilistic seismic hazard assessment (PSHA) has widely been used as a critical element for the determination of appropriate seismic design provisions for buildings and infrastructure (e.g., Bhatia et al. 1999; Kolathayar and Sitharam 2012; Ordaz et al. 2014; Ornthammarath et al. 2011; Sawires et al. 2016; Zhang et al. 1999). Implementing good seismic design provisions for buildings and other infrastructure is an effective way to reduce the seismic risk and thereby evading the earthquake-related disasters. The PSHA studies are primarily

[1] Key Laboratory of Continental Collision and Plateau Uplift, Institute of Tibetan Plateau Research, Chinese Academy of Sciences, Beijing 100101, China. E-mail: bailing@itpcas.ac.cn
[2] University of Chinese Academy of Sciences, Beijing 100049, China.
[3] Department of Petroleum and Mining Engineering, University of Jessore Science and Technology, Jessore 7408, Bangladesh.

Table 1

List of historical and major earthquakes ($M_w \geq 7.5$) in and around the study region since 1000 AD

Year	Lat.	Lon.	M_w	Ref.	Year	Lat.	Lon.	M_w	Ref.
9/29/1411	30.0	90.2	7.6	A&D	1/3/1911	43.5	77.5	7.7	NOAA
6/6/1505	29.5	83.0	8.1	A&D	8/4/1914	43.5	91.5	7.5	NOAA
6/27/1515	26.7	100.7	7.8	Z	8/28/1916	30.0	81.0	7.7	NOAA
3/29/1536	28.1	102.2	7.5	Z	12/16/1920	36.6	105.3	8.3	NOAA
8/31/1555	33.5	75.5	7.5	A&D	11/15/1921	36.5	70.5	7.8	NOAA
7/21/1654	34.3	105.5	8.0	Z	12/6/1922	36.5	70.5	7.5	NOAA
11/30/1663	25.0	90.0	7.7	A&D	5/22/1927	36.8	102.0	7.6	NOAA
10/14/1709	37.4	105.3	7.5	Z	1/27/1931	25.6	96.8	7.6	NOAA
11/30/1715	43.2	81.0	7.6	Z	12/25/1932	39.7	96.7	7.6	NOAA
6/19/1718	35.0	105.2	7.5	Z	8/25/1933	31.9	103.4	7.5	NOAA
8/2/1733	26.3	103.1	7.8	Z	1/15/1934	27.6	87.1	8.2	NOAA
6/1/1786	29.9	102.0	7.8	Z	5/30/1935	29.5	66.7	7.6	NOAA
9/1/1803	28.8	78.6	7.7	S	1/7/1937	35.5	97.6	7.5	NOAA
6/11/1806	28.5	92.0	7.6	A&D	11/2/1946	41.5	72.5	7.6	NOAA
3/8/1812	43.7	83.0	8.0	Z	3/17/1947	33.3	99.5	7.7	NOAA
12/8/1816	31.4	100.7	7.5	Z	7/29/1947	28.5	94.0	7.9	NOAA
8/26/1833	27.6	86.1	8.0	Z	3/4/1949	36.0	70.5	7.5	NOAA
9/6/1833	25.0	103.0	8.0	Z	8/15/1950	28.5	96.5	8.6	NOAA
2/19/1842	34.7	71.0	7.6	A&D	11/18/1951	31.1	91.4	7.5	NOAA
9/12/1816	27.7	102.4	7.5	Z	4/14/1955	30.0	101.8	7.5	NOAA
5/31/1871	28.0	91.5	7.5	Z	12/4/1957	45.5	99.5	8.1	NOAA
1/10/1889	24.0	93.3	8.3	Z	7/14/1973	35.2	86.5	7.5	NOAA
7/11/1889	43.2	78.7	8.3	Z	2/6/1973	31.4	100.6	7.6	NOAA
9/23/1896	37.0	71.0	7.5	B	8/23/1985	39.4	75.2	7.5	NOAA
6/12/1897	25.1	90.1	8.4	S	8/19/1992	42.1	73.6	7.5	NOAA
8/22/1902	39.9	76.2	7.7	NOAA	11/8/1997	35.1	87.3	7.5	NOAA
3/16/1902	39.9	76.2	8.3	Z	11/14/2001	35.9	90.5	7.8	NOAA
4/4/1905	33.0	76.0	8.6	NOAA	10/8/2005	34.5	73.6	7.6	NOAA
12/22/1906	43.5	85.0	8.3	NOAA	5/12/2008	31.0	103.3	7.9	NOAA
12/12/1908	26.5	97.0	7.5	NOAA	10/26/2015	36.4	70.7	7.5	NOAA
7/7/1909	36.5	70.5	8.1	NOAA	4/25/2015	28.1	84.7	7.8	NOAA
7/4/1911	36.0	70.5	7.6	NOAA					

A&D: Ambraseys and Douglas (2004); B: Bhatia et al. (1999); S: Szeliga et al. (2010); Z: Zhang et al. (1999); NOAA: National Oceanic and Atmospheric Administration

based on the earthquake catalogs (both instrumental and historical ones). In terms of time span, the duration of the complete part of the instrumental earthquake catalog is very short (e.g., around 55–60 years for this study region) compared to the duration of the tectonic processes required for earthquake generation (Bilham 2013). Using the short spanning earthquake catalog in PSHA may yield low hazard values for some regions, where great earthquakes have actually occurred and evident from the 2008 Sichuan M_w 7.9, the 2010 Haiti M_w 7.0, and 2011 Japan M_w 9.0 earthquakes (Wang et al. 2012). We, therefore, compile all available historical and instrumental earthquake catalogs, which include more data than the existing studies.

The seismic hazard maps for the Himalayan–Tibetan area have been previously studied since the 1990s (e.g., Bhatia et al. 1999; Zhang et al. 1999; Gao 2003). The GEM-faulted earth project carried out studies on the characterization of the Himalayan Frontal Thrust (MFT) active fault in appraising the attributes for seismic hazard and seismic risk for Himalaya region (Berryman et al. 2014). The occurrence of the major historical earthquakes in the Himalayan–Tibetan region (Table 1) varies remarkably on the basis of the seismotectonic settings of the study area. The frequency of earthquake occurrence in the Himalayan orogenic belt and the Tien Shan orogenic belt is much higher than that in the interior of the Tibetan plateau (Bai et al. 2017).

In this study, we use a methodology recently developed by Kijko et al. (2016) for the assessment of the key seismic hazard parameters, because it uses both historical and instrumental earthquakes for the estimation of spatio-temporal hazard variation. The seismicity parameters (e.g., γ, b value, M_{max}) are assumed to be constant over time and space by most of the PSHA procedures. However, the closer examination of earthquake catalogs indicates the significant variations of seismic activity rate and Gutenberg–Richter b value. The parameters are computed assuming the incompleteness of the event catalogs by accounting for historical records since the tenth century and complete instrumental records with different levels of completeness. In addition, the uncertainty of the earthquake-occurrence model and the determination of seismicity parameters are taken into account. Besides, three seismogenic source models (i.e., the smoothed-gridded seismicity, the linear source model, and areal source model) are combined by the use of a standard logic tree structure for capturing the model based epistemic uncertainties. In addition, two sets of ground motion prediction equations (GMPEs) are also selected for active shallow crustal and subduction interface earthquake regimes. This analysis produces a set of probabilistic seismic hazard maps for peak ground acceleration (PGA) and spectral acceleration (SA) for a better understanding about the spatial variation of seismic hazard value.

2. Data and Methods

2.1. Earthquake Catalogs

Earthquake catalog provides the fundamental basis for delineating the seismogenic sources and for assessing the key seismicity parameters, including the mean seismic activity λ, the b value of the frequency–magnitude Gutenberg–Richter relation, and M_{max}, the maximum expected earthquake magnitude of the study area. The incompleteness of the earthquake catalog is considered by accounting both historical earthquakes and instrumental catalog with different levels of completeness (Kijko and Smit 2012; Kijko et al. 2016). To prepare a composite earthquake catalog, we have collected historical earthquake archives for Tibetan–Himalayan region as much as possible. Lee et al. (1976) is one of the biggest historical earthquake repositories for China mainland, which even contains the information about pre-historic earthquakes. For Himalaya and adjacent region, Ambraseys and Douglas (2004) and Szeliga et al. (2010) are the prime sources for the historical major earthquakes. Besides, the historical earthquake records from the National Oceanic and Atmospheric Administration (NOAA), GEM Global Historical Earthquake Archive (GEM-GHEA), and the National Seismological Centre of Nepal (NSC) are used. For instrumental seismic-event catalogs, the earthquake records from the U.S. Geological Survey (USGS), International Seismological Centre (ISC), and China Seismograph Network (CSN) between 1906 and 2016 are utilized.

To obtain the comprehensive catalog, the catalogs from different sources are then assembled together and checked manually for removing the duplicate earthquakes on the basis of location, time, and magnitude. Different types of magnitude scaling (e.g., body wave magnitude, surface wave magnitude, duration magnitude, and local magnitude) contained in the catalog are converted into moment magnitude (M_w) scaling using the formulas, as shown in Table 2. About 30,000 events are recorded in the comprehensive catalog with magnitude $M_w \geq 4.0$ including the

Table 2

Magnitude scaling relations used for conversion of different types of magnitude scaling into moment magnitude scale

Scordilis (2006)	Grünthal and Wahlström (2003)	Kaviris et al. (2008)
$M_w = 0.67\ M_S + 2.07$ for $3.0 \leq M_S \leq 6.1$ $M_w = 0.99\ M_S + 0.08$ for $6.2 \leq M_S \leq 8.2$ $M_w = 0.85\ M_b + 1.03$ for $3.5 \leq M_b \leq 6.2$	$M_w = 0.67(\pm 0.11) + 0.56(\pm 0.08)$ $M_L + 0.046(\pm\ 0.013)\ M_L^2$	$M_w = M_D + 0.5$ ($M_D < 3.0$) $M_w = M_D + 0.6$ ($M_D \geq 3.0$)

M_w moment magnitude, M_S surface wave magnitude, M_L local magnitude, M_b body wave magnitude, M_D duration magnitude

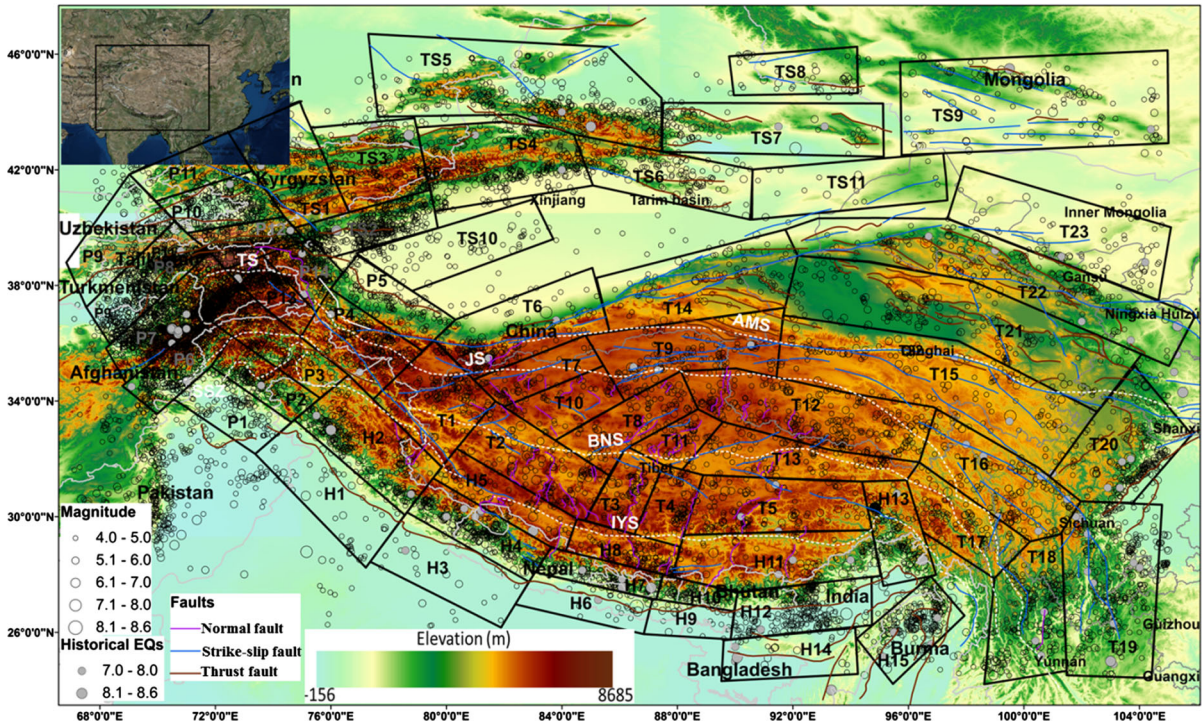

Figure 1

Location map showing the distribution of instrumental (*black open circles*) and major historical (*grey filled circles*) earthquake epicenters. Active faults are adopted from Styron et al. (2010). *Dotted white lines* are suture zones: *IYS* Indus Yalu suture zone, *BNS* Bangong Nujiang suture zone, *JS* Jinsha suture zone, *SSZ* Shyok suture zone, *TS* Tanymas suture zone, *AMS* Anyimaqen–Kunlun–Muztagh suture zone. *Black rectangles* are seismic source zones. Insert is the map of East Asia and surrounding countries, while the *marked rectangle* within the insert map is the study region

historical earthquakes. Since the seismicity model assumes that the occurrence of an earthquake is independent, a declustering process following the algorithm of Gardner and Knopoff (1974) is performed to exclude the effects of foreshocks and aftershocks. A total of 12,000 events are included in the final catalog (Fig. 1).

For instrumentally recorded earthquake catalog, it is very important to assess the different levels of completeness of various sub-catalogs, because the large earthquake records are generally complete rather for longer periods than the smaller earthquakes. The completeness of earthquake catalog is usually associated with the socio-economic and historical aspects, the demographic variations, and the seismic station coverage. If the incompleteness of the catalog is not taken into account, the recurrence rates would be overestimated and underestimated for small and large earthquakes, respectively. To estimate the completeness of the earthquake catalog, we use visual cumulative method (Tinti and Mulargia 1985) and assume a threshold magnitude (M_0) of M_w 4.0. The catalog is found to be complete from 1964 onwards for Himalaya and Pamir–Hindu Kush regions (Fig. 2a) and from 1960 onwards for Tibetan and Tien Shan regions. This implies that the catalog before the modern instrumental period is incomplete typically for small magnitude earthquakes. To incorporate the entire instrumental earthquake catalog since 1906, different complete time windows for various magnitude intervals (e.g., 4.0–5.0; 5.0–6.0; and 6.0–7.0) which corresponds to different complete sub-catalogs that are assessed employing the statistical method of Stepp (1972). For example, in the Himalayan region, the different levels of completeness are of 4.0, 5.0, and 6.0 with the corresponding complete time windows that are of 1964 onwards, 1925–1964, and 1906–1925, respectively (Fig. 2b).

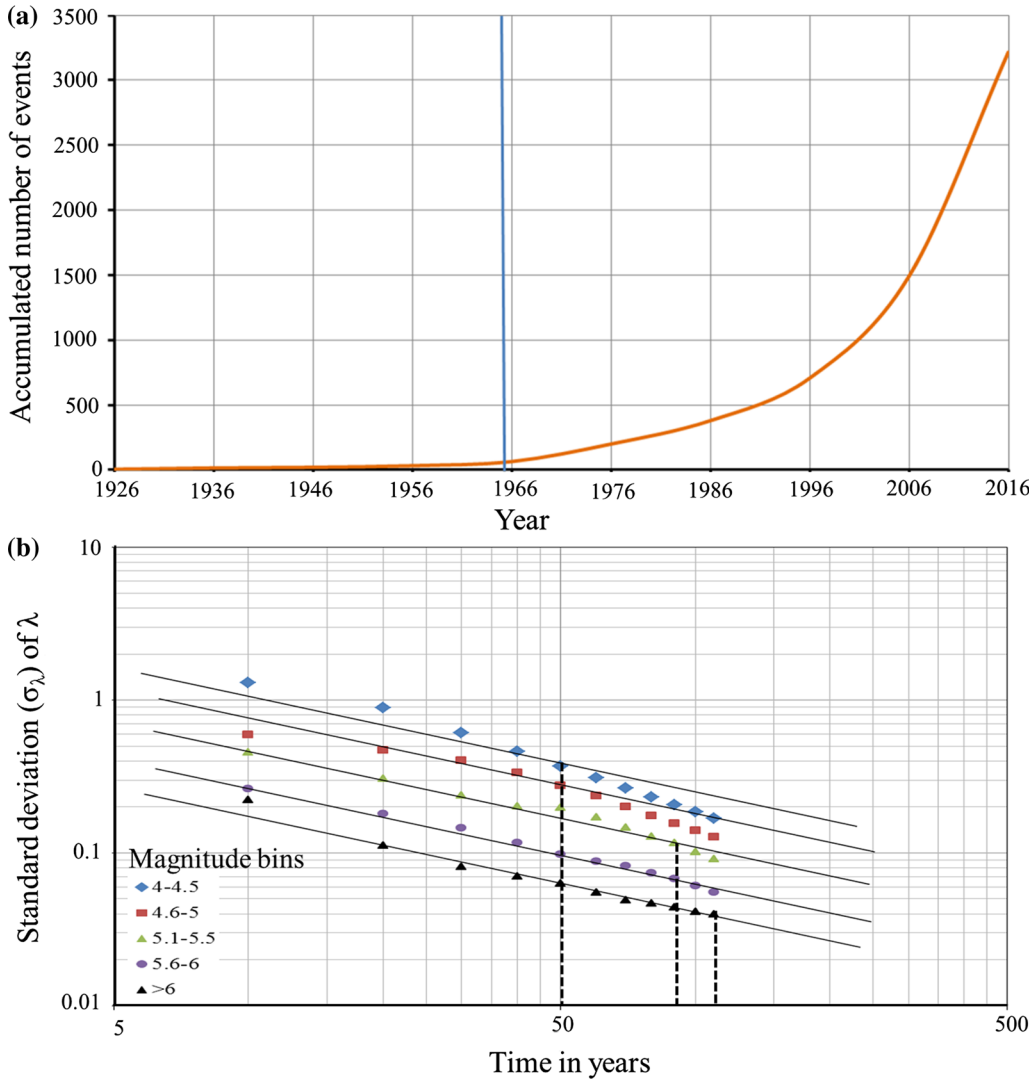

Figure 2
Example of **a** completeness verification for $M_0 = 4.0$ and **b** different complete time windows for the corresponding magnitude intervals (*solid tangent lines* show the constant standard deviation and *vertical dashed lines* show the length of the time interval) for Himalayan orogenic belt

2.2. *Earthquake Source Models*

Proper seismic source zone identification and delineation is very important in PSHA. Seismic zones are usually defined by considering on the tectonic environment, seismological and geological attributes. The study region is regarded as complex tectonic environment in producing the earthquakes. This analysis thus used a model built from a combination of three different seismic source materials: areal, linear, and smoothed-gridded sources.

2.2.1 *Areal Seismic Sources*

The basic principle used in delineating the area of seismic source zones requires that seismicity within a single source zone must remain uniform and homogenous. Therefore, every point within the source is assumed to have an equal potential for the generation of an earthquake in the future. The standard Cornell approach (Cornell 1968) is primarily based on seismic areal sources. Seismicity distribution, geological behaviors, active fault characteristics,

seismotectonic settings, and focal mechanism of earthquakes are the principal criteria to delineate the seismic areal source zone. Based on these criteria and zones on the previous studies (e.g., Bhatia et al. 1999; Nath and Thingbaijam 2012; Zhang et al. 1999; Zhangming 1992), 63 areal source zones are identified for the whole study area. High seismicity clusters are present in Pamir–Hindu Kush region, western Nepal, east-central Nepal, eastern Himalayan syntaxis, and central to west of Tien Shan. Interior of Tibet shows moderate seismicity, while the Tarim basin shows very sparse seismicity (Fig. 1).

2.2.2 Linear Seismic Sources

The major active faults are considered as linear seismic sources, because major earthquakes are mostly associated with these faults. The active faults identified from the remote sensing imagery, aerial photographic interpretation, paleoseismic studies, and field investigations (Styron et al. 2010) are used in this study. For the whole study region, the identified numbers of normal, strike slip, and thrust faults are of 50, 69, and 119, respectively (Fig. 1). The empirical relationships are applied to characterize the parameters of faults if it is not well constrained by other studies. For magnitude–area and magnitude–length scaling relationships, two different regression relationships are adopted: Yen and Ma (2011) and Wells and Coppersmith (1994). Stirling and Goded (2012) carried out a compilation and evaluation on 72 magnitude–area and magnitude–length scaling relationships. They found that the quality of the relationships of Yen and Ma (2011) is better than that of Wells and Coppersmith (1994) because of updated wide-spread data sets with large magnitude coverage, and the assigned quality score is of 1 (best available). On the other hand, they recommended the quality score of 2 (good) for Wells and Coppersmith (1994) relationships because of old data sets and relatively narrow magnitude coverage. Accordingly, in this analysis, two-third and one-third weightages are assigned to Yen and Ma (2011) and Wells and Coppersmith (1994), respectively. The occurrence rate of large magnitude earthquakes along these faults is determined using long-term slip rates as

$$\text{Recurrence Interval} = M_0/\mu\dot{u}LW, \qquad (1)$$

where μ is shear modulus, 3.0×10^{11} dyne/cm^2, L is rupture length, W is rupture width, $\dot{u}$ is the fault slip rate, and M_0 is the seismic moment which is directly related to magnitude (M) as Hanks and Kanamori (1979):

$$Log(M_0) = 1.5M + 16.05. \qquad (2)$$

As the attributes (e.g., dip, slip, and slip rate) of small-scale faults are not well-documented, we assign the same values for the above-mentioned parameters taken from the nearby known faults to small-scale faults. The Main Frontal Thrust (MFT) is one of the well-constrained active faults in the study area. The slip rate of the MFT is studied from the GPS observations (Ader et al. 2012). The attributes of the MFT at three different segments are derived by the GEM-faulted earth project (Berryman et al. 2014); which are directly used in this study. The Characteristic-earthquake magnitude–frequency distribution model for the empirically estimated earthquakes with magnitude equal to or higher than M_w 6.5 and Gutenberg–Richter magnitude–frequency distribution model for instrumentally recorded earthquakes are used in linear source model. Table 3 shows an example illustrating the linear source parameters (e.g., seismic moment, slip rates, rupture length, and rupture) for Himalayan region.

2.2.3 Smoothed-Gridded Seismicity

Due to the wide scattering of earthquake hypocenters in relation with fault locations, a zone-free approach (Frankel 1995; Woo 1996) is used for the spatial smoothing of seismicity to avoid any subjectivity for delineating areal seismic sources. This zone-free approach is also called the kernel estimation method, because it implements the spatial smoothing of seismicity and depicts the non-uniform spatial distribution of seismicity assuming that it varies from place to place. For smoothed gridded, the study area is divided into thousands of grids with the size of $0.1° \times 0.1°$. Earthquakes of $M_w \geq 4.0$ are counted in each grid square for different magnitude intervals to estimate the occurrence rates for the corresponding magnitude intervals. The calculated seismicity rates are then smoothed to get the final activity rate

Table 3

Examples showing parameters of active faults in Himalayan region estimated in this study

Fault name	Length (km)	M_0*	Width (km)	Slip rate (mm/year)	b	σ_b	λ
MFT-1	1300	2.67888E+22	100	20.5	0.76	0.09	4.334
MFT-2	330	1.6133E+21	100	18.0	0.61	0.04	2.703
MFT-3	800	9.86865E+21	100	20.0	0.73	0.09	1.371
Tibrikot	62	5.50155E+19	39	20.5	0.69	0.14	0.055
Humla	76	8.27582E+19	47	20.5	0.61	0.13	0.370
Tingri	44	2.77124E+19	30	18.0	0.51	0.1	0.233
Kung Co	68	6.62049E+19	43	18.0	0.44	0.09	0.090
hf1	70	7.01679E+19	44	20.5	0.54	0.12	0.154
hf2	55	4.32837E+19	36	20.5	0.55	0.22	0.048
hf3	65	6.04792E+19	41	20.5	1.2	0.12	0.164
hf4	139	2.79178E+20	76	20.5	0.69	0.16	0.425
hf5	92	1.21496E+20	54	18.0	0.71	0.1	0.223
hf6	179	4.65654E+20	93	18.0	0.63	0.1	0.148
hf7	103	1.52508E+20	60	18.0	0.48	0.1	0.066
hf8	82	9.64029E+19	50	18.0	0.54	0.21	0.102

Fault numbering (hf1–hf8) is chosen arbitrary since no naming for these faults are shown before. Rupture width for MFT-1–MFT-3 is taken from (Berryman et al. 2014) and for the rest of the faults are from (Yen and Ma 2011). Slip rates are recorded from (Ader et al. 2012). λ, b value, and σ_b are used for Gutenberg–Richter seismicity model. M_0* is the weighted seismic moment

adopting the multivariate Kernel probability density function using the equation (Woo 1996):

$$\hat{n}_i = \frac{\sum_j n_j e^{-\Delta_{ij}^2/c^2}}{\sum_j e^{-\Delta_{ij}^2/c^2}}, \tag{3}$$

where n_j is the rate of seismicity in the jth grid cell, $\hat{n}_i$ is the smoothed rate of seismicity in the ith cell, c is the correlation distance accounting for location uncertainties, and Δ_{ij} is the distance between the ith and jth cells. The sum is taken over cells j within a distance of $3c$ of cell i. At present, there are no complete rules or guidelines in determining the appropriate c value. For very small c value, the resulting smoothed seismicity will be concentrated around the epicenters of the recorded earthquakes, while larger c value spreads out the seismicity and does not reflect the true spatial variation of seismicity as assumed in zone-free approach. Therefore, we assign c value as 0.5° according to Frankel (1995).

2.3. *Maximum Magnitude and Focal Depths of Earthquakes*

The maximum expected earthquake magnitude (M_{max}) for every seismic source zone is computed using historical and recent earthquake data, as well as the largest magnitude earthquakes that occurred in nearby seismic zones with similar tectonic settings following the algorithm of Kijko and Singh (2011) by taking into account the uncertainty in the earthquake magnitude determination. The maximum expected magnitude of earthquake along its uncertainty for all areal source zones is given in Table 4. It is found that most of the zones along the central Himalaya are with high M_{max} values and reach as high as 8.6, while the dominant portion in the interior of Tibetan plateau shows low (as low as 6.5)-to-medium value. The computed M_{max} value varies between 8.6 and 6.5. For smoothed-gridded seismicity, the same range of M_{max} is used.

Accurate determination of earthquake locations for the study area is usually difficult because of the insufficient station coverage. Earthquakes listed in the ISC catalog appear to be distributed throughout the thickness of the Tibetan and Indian crust range between 0 and 90 km. However, recent studies have shown that most of the earthquakes in Himalaya are concentrated at depths ranging between 10 and 20 km (Pandey et al. 1999; Priestley et al. 2008). In addition, the average focal depth for the Gorkha earthquake sequence is $\sim$15 km estimated using waveforms from a nearby broadband seismic array (Bai et al. 2016). In Tibetan plateau, the focal depths for most of the events range from 0 to 40 km (Bai et al. 2012)

Table 4

Computed seismicity parameters for areal source zones

Zones	λ*	β	SE_β*	M_{max}	SE_{Mmax}*	Zones	λ*	β	SE_β*	M_{max}	SE_{Mmax}*
H1	0.73	1.81	0.21	7.4	0.27	T4	0.89	1.32	0.18	7.41	0.35
H2	1.76	1.47	0.09	8.3	0.26	T5	1.15	1.35	0.12	8.2	0.26
H3	0.37	1.31	0.23	8.2	0.31	T6	2.89	1.48	0.1	7.81	0.31
H4	1.75	1.29	0.08	8.2	0.26	T7	0.66	1.39	0.23	6.66	0.27
H5	0.98	1.57	0.15	8.7	0.33	T8	1.06	1.24	0.18	6.8	0.26
H6	0.53	1.48	0.17	8.7	0.42	T9	2.40	1.22	0.14	6.71	0.26
H7	1.26	1.31	0.11	8.5	0.27	T10	0.88	1.24	0.26	6.3	0.26
H8	1.31	1.28	0.18	6.5	0.26	T11	0.84	1.29	0.14	6.38	0.25
H9	0.49	1.25	0.08	5.95	0.29	T12	2.08	1.19	0.09	7	0.26
H10	1.48	1.32	0.17	7.05	0.27	T13	1.77	1.61	0.18	6.29	0.25
H11	1.19	1.44	0.13	8.3	0.27	T14	1.13	1.21	0.16	7.31	24
H12	1.91	1.34	0.1	7.71	0.26	T15	1.62	1.42	0.12	8.3	0.41
H13	1.86	1.35	0.1	9.09	0.74	T16	1.22	1.52	0.11	8	0.25
H14	2.22	1.19	0.09	8	0.28	T17	1.12	1.34	0.17	6.66	0.26
H15	0.39	1.25	0.18	8.9	0.4	T18	1.00	1.58	0.1	8.3	0.29
P1	2.08	1.35	0.19	6	0.25	T19	1.12	1.51	0.08	8.5	0.28
P2	1.68	1.46	0.11	7.9	0.26	T20	0.85	1.54	0.1	8.5	0.31
P3	3.40	1.21	0.09	7.51	0.22	T21	0.92	1.52	0.13	7.51	0.25
P4	2.87	1.53	0.1	7.9	0.26	T22	0.77	1.66	0.11	8.4	0.35
P5	2.27	1.25	0.11	6.71	0.25	T23	0.97	1.66	0.22	7.61	0.25
P6	3.23	1.43	0.07	8.3	0.24	TS1	1.51	1.62	0.14	7.05	0.21
P7	6.88	1.34	0.04	8.3	0.26	TS2	4.77	1.29	0.07	8.8	0.27
P8	5.71	1.33	0.06	7.91	24	TS3	1.89	1.49	0.1	8.8	0.26
P9	1.23	1.32	0.13	7	0.25	TS4	2.42	1.53	0.08	8.1	0.25
P10	1.87	1.60	0.11	7.11	0.24	TS5	2.35	1.63	0.09	8.3	0.26
P11	1.10	1.31	0.17	8.1	0.69	TS6	2.65	1.42	0.13	7.05	0.26
P12	4.39	1.45	0.13	7.61	0.25	TS7	0.87	1.63	0.17	7.91	0.25
P13	2.93	1.29	0.08	7.81	0.27	TS8	0.62	1.43	0.25	7.5	0.75
P14	2.28	1.48	0.1	7.6	0.25	TS9	1.52	1.26	0.13	8.5	0.67
T1	1.59	1.52	0.1	6.82	0.26	TS10	1.24	1.24	0.23	6.59	0.28
T2	1.40	1.29	0.13	7.31	0.26	TS11	0.29	1.34	0.45	7	2.49
T3	0.89	1.22	0.18	7.41	0.35						

λ* is the rate of seismicity; SE_β* is the standard error of beta; SE_{Mmax}* is the standard error of M_{max}. The average focal depths of source zones H1–H15, P1–P14, T1–T23, and TS1–TS11 are 15, 25, 20, and 15 km, respectively

and 0 to 50 km (Sloan et al. 2011). In particular, moderate-to-large earthquakes are mostly shallower than 30 km in the northern Tibet and shallower than 20 km in the central and southern Tibet (Bai et al. 2017). The earthquakes occurred in Tien Shan are mostly limited within the depths ranging between 0 and 30 km (Khan et al. 2017; Sloan et al. 2011). In this analysis, the average focal depth (e.g., 15 km in Himalaya and Tien Shan) of each seismic belt is assigned as a constant depth for all source models.

2.4. Seismicity Model and Parameters

To calculate earthquake magnitude exceedance rates, a Modified Gutenberg–Richter (MGR)–Poisson model is selected as a seismicity model for all seismogenetic sources except characteristic earthquakes. Herein, the seismicity is expressed as (Cornell and Van Marke 1969)

$$\lambda(M) = \lambda_0 \frac{\exp(-\beta M) - \exp(-\beta M_{\max})}{\exp(-\beta M_0) - \exp(-\beta M_{\max})}, \quad M_0 \le M \le M_{\max}, \tag{4}$$

where λ_0 is the rate of earthquake activity with threshold magnitude M_0 (here, $M_0 = 4.0$), β is a parameter equivalent to the b value ($\beta = 2.303 \times b$), and M_{max} is the maximum expected magnitude for the sources. The uncertainty of both M_{max} and β is taken into account in computing the $\lambda(M)$ value.

Traditionally, the seismicity parameters are calculated based on the minimum magnitude of completeness (M_c). The evaluation of M_c is conducted using the Maximum Curvature (MAXC) method (Wiemer and Wyss 2000). The estimated M_c value is $\sim M_w$ 4.0 and this value is taken as threshold magnitude (M_0), because earthquakes smaller than M_w 4.0 are not likely to cause any damage to infrastructure from engineering point of view. In this study, the essential seismicity parameters are computed taking into account the incompleteness of the instrumental catalog and the historical earthquake records since the tenth century. The Gutenberg–Richter b value and its standard error for every seismic belt and areal source zone are computed using the joint likelihood function of Kijko et al. (2016) by accounting the incomplete historical and complete parts of the catalog. This newly developed method takes into account both incompleteness of the seismic catalogs and temporal variation of seismicity. This procedure applies a Bayesian Poisson–gamma distribution as a model of earthquake occurrence in time and a Bayesian Exponential–gamma distribution as a model of earthquake magnitude. We create the Poisson–gamma compound distribution to obtain the probability for the observed n seismic events, within a time interval t, for temporal varying seismic activity λ (Benjamin 1968), as follows:

$$P_n(\bar{\lambda}, t, v_\lambda) = \int_0^\infty P_n(\lambda, t) f_\Delta(\lambda) \mathrm{d}\lambda = \frac{\Gamma(n+q_\lambda)}{n!\Gamma(q_\lambda)} \left(\frac{p_\lambda}{t+p_\lambda}\right)^{q_\lambda} \left(\frac{t}{t+p_\lambda}\right)^{n}, \quad (5)$$

in which $\Gamma(n)$ is the gamma function, p_λ and q_λ are the parameters of gamma distribution, such that $p_\lambda = \bar{\lambda}/\sigma_\lambda^2$, $q_\lambda = \bar{\lambda}^2/\sigma_\lambda^2$, and $\bar{\lambda}$ denote the mean value of the activity rate λ.

The applied models make it possible to incorporate the uncertainty associated with randomly, time-varying seismicity. It is observed that the overall b value using this algorithm is rather lower than that of traditionally used algorithm of Aki (1965). For Himalaya, Pamir–Hindu Kush, Tien Shan and Tibet regions, the estimates of β value are of 1.50, 1.53, 1.49, and 1.48, respectively. In Table 4, the β values and their standard errors are given for all the areal source zones. Worth mentioning that in smooth-gridded seismicity model, the exact same β value is assigned to all grids within the each seismic belt. The average annual rate of seismicity (λ_0) at threshold magnitude for each seismic source zone is computed using the method of likelihood function (Kijko et al. 2016) assuming the Poisson–gamma compound distribution of the earthquake magnitude–frequency as

$$L_i(\bar{\lambda}|n_i, t_i) = \left(\bar{\lambda}^{(i)} t_i + q_\lambda\right)^{-q_\lambda} \left(\frac{\bar{\lambda}^{(i)} t_i}{\bar{\lambda}^{(i)} t_i + q_\lambda}\right)^{n_i}, \quad (6)$$

where $\bar{\lambda}^{(i)}$ is the mean earthquake activity rate of the ith sub-catalog, corresponding to the magnitude level of completeness $m_{\min}^{(i)}$.

2.5. *Selection of Ground Motion Prediction Equations*

Attenuation relations, i.e., the ground motion prediction equations (GMPEs), are required for the estimation of ground motion parameters (e.g., PGA and SA). These can be used to calculate the probability distribution of ground motion intensity as a function of various variables such as earthquake magnitude, source-to-site distance, and soil condition. These relationships are usually obtained empirically using a statistical regression method on a particular set of strong-motion parameters.

The seismotectonic setting of the Himalayan–Tibetan region is very complex. This study area is a tectonically active interplate region (Nath and Thingbaijam 2012), where the earthquake-occurrence environment is not simple and rather even compound in combination. According to the study of Nath and Thingbaijam (2012), the Himalaya orogenic belt, Tien Shan and Tibet regions are belonged to the active shallow crustal regime (ACR) with many subduction interface zone (SIZ) earthquakes across the Himalaya. Studies on focal depths and focal mechanisms of earthquakes (Bai et al. 2017) stated that earthquake occurrence in this region is fairly associated with subduction interface. Most of the zones in Pamir–Hindu Kush region are regarded as SIZ. Moreover, some previous seismic hazard studies assumed that the Himalaya and its

surrounding region belong to either SIZ (e.g., Pandey et al. 2002) or ACR (e.g., Ram and Wang 2013), or both (e.g., Chaulagain et al. 2015). To avoid the controversy, in this study, we consider that Himalaya and Pamir–Hindu Kush regions are characterized with both ACR and SZI environments, while the Tibetan plateau and Tien Shan are belonged to ACR. For Tibetan–Himalayan region, there is no adequate number of strong-motion data and consequently no particular GMPEs yet and even not enough to check the validity and compatibility of the GMPEs from the other regions.

The usual practice to resolve the problem is to select the GMPEs developed in other regions with similar seismotectonic settings which could represent adequately the ground motion in this region. Therefore, following the criteria (e.g., tectonic regime, journal types, data sets, frequency range of the model, functional form, regression coefficients, etc.) of Cotton et al. (2006), and performing a number of trellis plots [i.e., predicted spectral acceleration (PSA) versus magnitude, PSA versus distance, and PSA versus structural periods] according to Stewart et al. (2013), a total of eight GMPEs are selected in this analysis. Four of them are for the ACR and the other four for the SZI. For ACR, the selected models include two Next-Generation Attenuation (NGA-west2) models developed by Abrahamson et al. (2014) and Chiou and Youngs (2014) using the global data sets, one model applicable for Europe and Middle East by Ambraseys et al. (2005), and Zhao et al. (2006) mostly using Japanese data. Due to scarcity of strong-motion records in Himalayan–Tibetan region, the weight assessment and, thereby, the ranking of different GMPEs are not computed in this study. Many of the seismic hazard studies for Asian countries (e.g., Chaulagain et al. 2015; Kolathayar and Sitharam 2012; Nath and Thingbaijam 2012; Ornthammarath et al. 2011) used equal weight for all models due to insufficient observed data. Therefore, equal probabilistic weights (1/4) are assigned to each of these four models. On the other hand, for SIZ with the large distance, we employed three models from global data sets, namely, the BC Hydro 2016 known as Abrahamson et al. (2016), Atkinson and Boore (2003), and the Youngs et al. (1997), and another one from local data sets is of Zhao et al. (2006). Similar to ACR, equal probabilities (1/4) to each of the models are used.

Compatibility among these selected GMPEs is checked when applied in the CRISIS2015 (Ordaz et al. 2015) program. This program allows the use of different distance definitions (e.g., Joyner–Boore, rupture, and hypocentral distance) for different GMPEs. Moreover, the focal depth is taken into account as an independent variable. The assessment is carried out assuming rock-site condition (where the average V_{s30} is equal to 760 m/s). However, for Himalaya and Pamir–Hindu Kush regions, we combine two sets of GMPEs assigning equal weighting factor (0.5) in the logic tree. Besides, GMPEs for ACR are employed for the rest part of the study area. In the similar way, GMPEs are employed for all three source models.

2.6. Logic Tree Structure

Uncertainties are usually associated with the models used in PSHA. The use of logic tree allows capturing the epistemic uncertainties in different input models (Bommer et al. 2005; Sabetta et al. 2005) by including alternative models in the hazard computation. In this study, three types of seismogenic source models and two sets of GMPEs (each consisted of four different GMPEs) are considered. Equal weights (1/3) are assigned to each of the source models, as there is no substantial observed data for ranking the weight of the models. For linear source model, similarly, equal weights (1/2) are used for Characteristic-earthquake and Gutenberg–Richter seismicity models, because there is no specific reason to prefer one over another. Figure 3 shows the representation of the standard logic tree framework used for linear source model in the Himalaya, and Pamir–Hindu Kush regions.

2.7. Seismic Hazard Estimation

To predict the seismic hazards for future earthquakes, the seismic hazard module CRISIS2015 (Ordaz et al. 2015) is used because of its high efficiency of calculation and flexibility in model selection (Danciu et al. 2010). For areal and linear seismic sources, CRISIS computes the seismic hazard based on the standard Cornell approach (Cornell 1968). It assumes

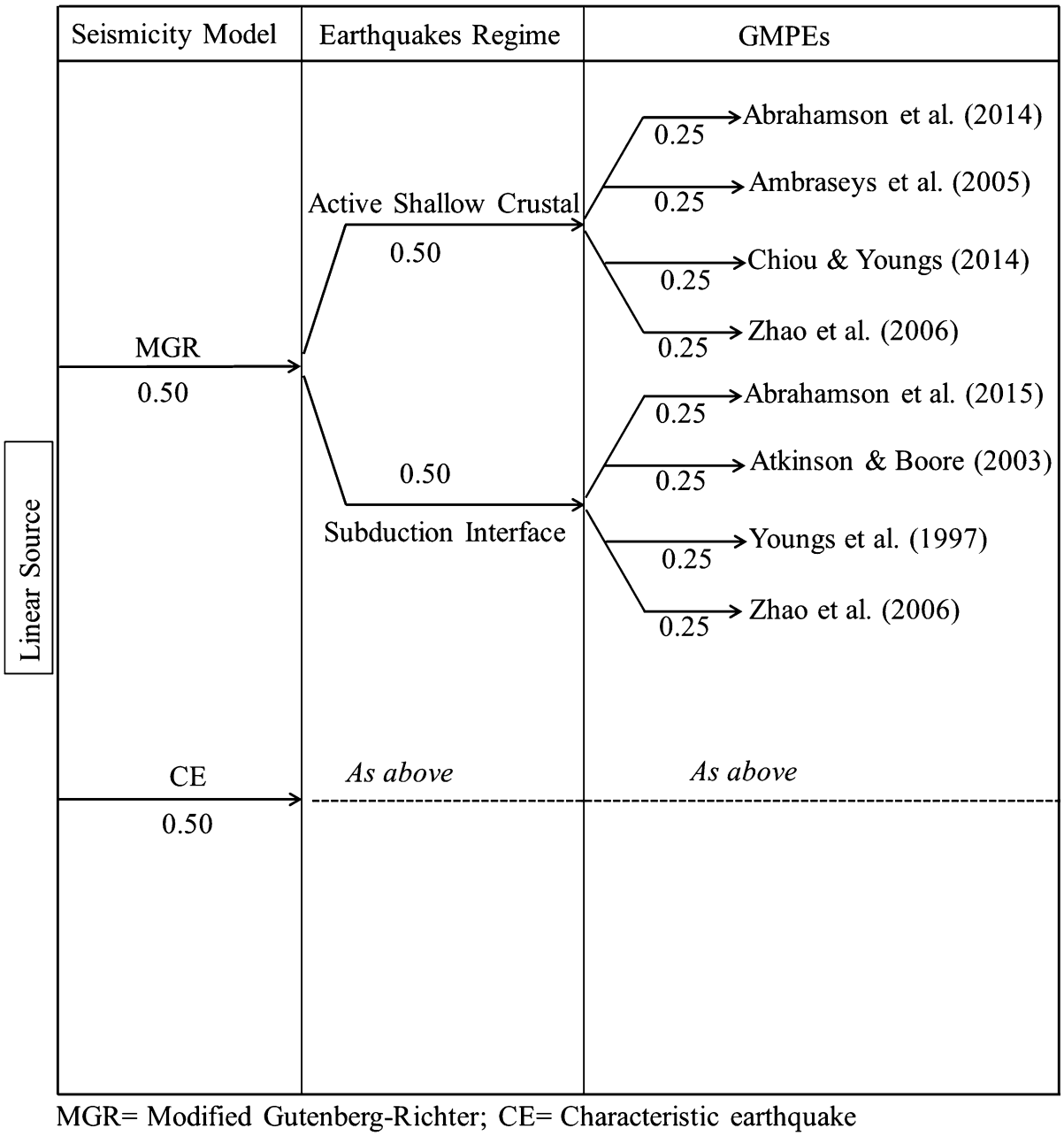

Figure 3
Logic tree structure for active linear seismogenic source model

that within a source, seismicity is evenly distributed by unit area and all points could be a potential earthquake focus. To obtain accurate hazard values, CRISIS performs a spatial integration by subdividing the original sources. Once a source is subdivided into sub-sources, the acceleration exceedance rate due to the *i*th single source can be computed using the equation:

$$v_{i(a)} = \sum_j W_{ij} \int_{M_0}^{M_{\max}} \left(-\frac{\mathrm{d}\lambda(M)}{\mathrm{d}M} \right) \Pr\left(A > a | M, R_{ij}\right) \mathrm{d}M, \tag{7}$$

where M_0 and $M_{\max}$ are the threshold and maximum magnitudes, respectively; $\Pr\left(A > a | M, R_{ij}\right)$ is the

probability that the acceleration exceeds a certain value a at the site across distance R_{ij} for an earthquake with magnitude M, and W_{ij} is the weight of each sub-element. The above expression also assumes that $\sum W_{ij} = 1$. The total average acceleration exceedance rate at the site due to the contributions of all the sources, N, within 300 km is calculated as

$$v(a) = \sum_{n=1}^{N} \int_{M_0}^{M_{\max}} \left(-\frac{\mathrm{d}\lambda(M)}{\mathrm{d}M} \right) \Pr\left(A > a | M, R_{ij}\right) \mathrm{d}M. \tag{8}$$

For smoothed-gridded seismicity, once the seismicity parameters and the GMPEs are known for each of the nodes of the grids, the hazard at a given node is calculated based on the effects of the totality of the nodes and their corresponding distances to the site of interest, as shown in Eqs. (7) and (8).

3. Results and Discussion

For seismic hazard prediction, the entire study region is divided into small grids with the size of 0.1° × 0.1°. At the center of each grid cell, the PGA and SA values are assessed based on a referenced bedrock-site condition. The contribution to hazard value of all the potential sources within the radial distance of 300 km from the center of each gird cell is taken into account. This hazard estimation is performed by disaggregating the hypocentral distance into small intervals of 1 km and the magnitude range (between the minimum and maximum magnitudes) into small incremental values of 0.1. This analysis produces different seismic hazard maps of PGA and SA at short (0.2 s) and long (1.0 s) natural periods at 5% critical damping factor for 10 and 2% probabilities of exceedance in 50 years, corresponding to 475 and 2475 year return periods, respectively. Figure 4a, b depicts the hazard maps of PGA value for the probabilities of exceedance of 10 and 2%, respectively, in 50 years. The spatial variations of SA values obtained at 0.2 and 1.0 s natural periods for 2% probability of exceedance are presented in Fig. 5a, b, respectively.

The predicted hazard parameters in terms of both PGA and SA show a non-uniform spatial variation. In addition, a significant hazard-level variation is observed from 10% probability of exceedance to 2% probability of exceedance. Due to the heterogeneous nature of the seismotectonic settings of the study region, the produced seismic hazard maps show many low-and-high hazardous patches. The hazard distribution pattern thus nearly follows the background seismicity distribution over the study area and the areas of highest potential hazard are likely distributed along the Indian–Eurasian plate collision zones. However, for 10% probability of exceedance at 50 years, the minimum and maximum PGA values are found as low as 0.04 g and as high as 0.87 g, respectively (Fig. 4a). The Pamir–Hindu Kush region, where both shallow and intermediate seismic activities are high (Bai and Zhang 2015) and many earthquakes of $M_w \geq 7$ have occurred during the last century, is likely to be experienced the highest seismic hazard potential which is in the order of 0.67–0.87 g.

Along the entire Himalayan orogen specially the central segment, the resulting seismic hazard value is comparatively high (as high as 0.67 g) from existing studies and does agree with the results of some geodetic and paleoseismic studies (e.g., Ader et al. 2012; Avouac et al. 2015; Bilham 2015; Bollinger et al. 2016; Rajendran et al. 2015; Sapkota et al. 2013). All of these studies expected high seismic hazard potential in this region which has also raised the concerns of high seismic risk. It is essential to note that the MFT is the most potential source for future devastating earthquakes in Himalaya orogen, but the predicted hazard value is not as high as in central segment. In PSHA, hazards are computed considering the influence from earthquakes with possible magnitudes at all significant distances from the site of target. Besides, the level of hazard also depends on the rate of earthquake occurrence. Along the MFT, the recurrence interval of the great earthquake is ~700 years (Rajendran et al. 2015; Sapkota et al. 2013), whereas, in central Himalaya, the rate of seismicity is very high, although most of the earthquakes are medium to small in size. Therefore, these might be the plausible reasons for having comparatively lower values along MFT.

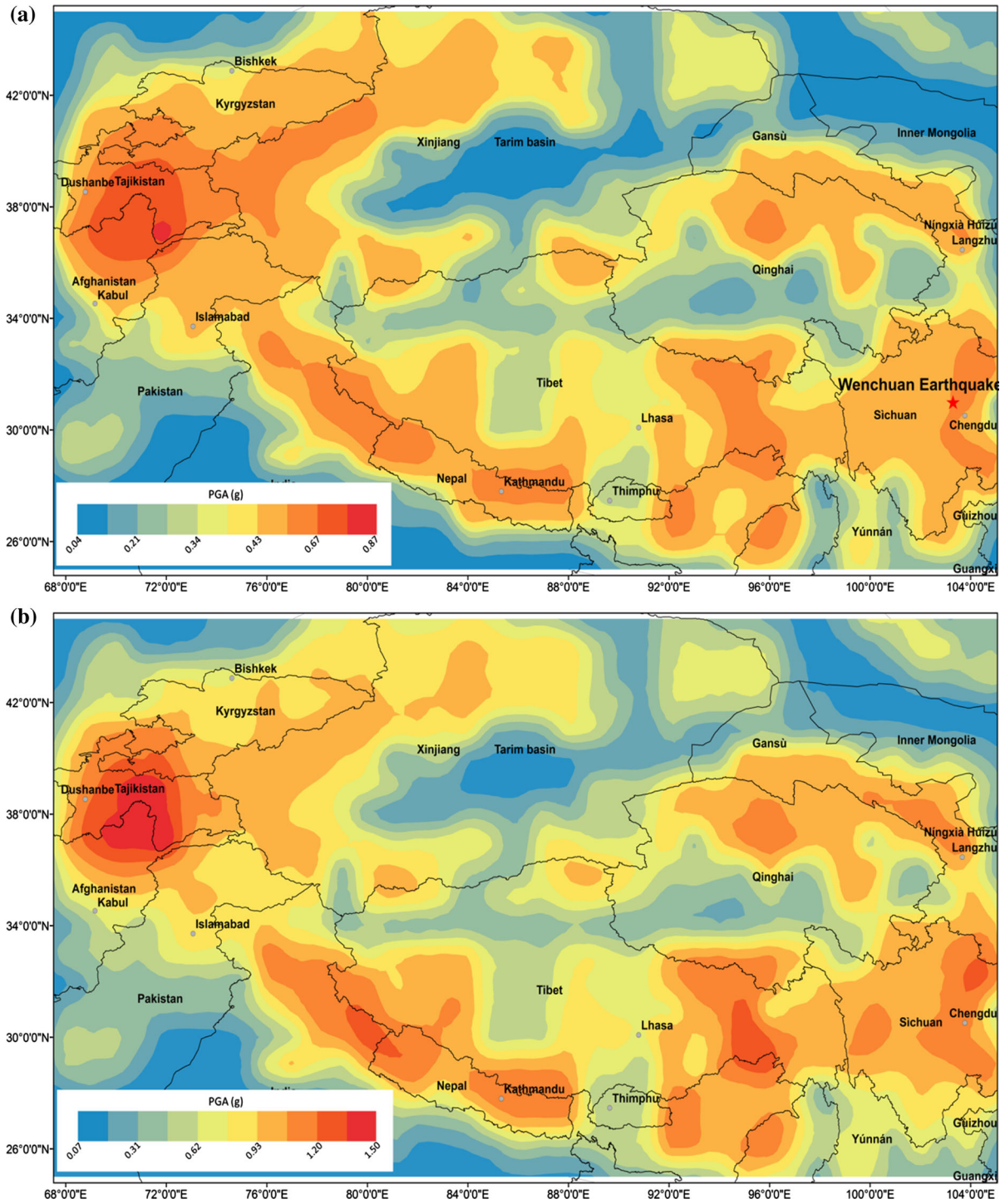

Figure 4
Spatial variation of PGA values for **a** 10% probability of exceedance and **b** 2% probability of exceedance in 50 years

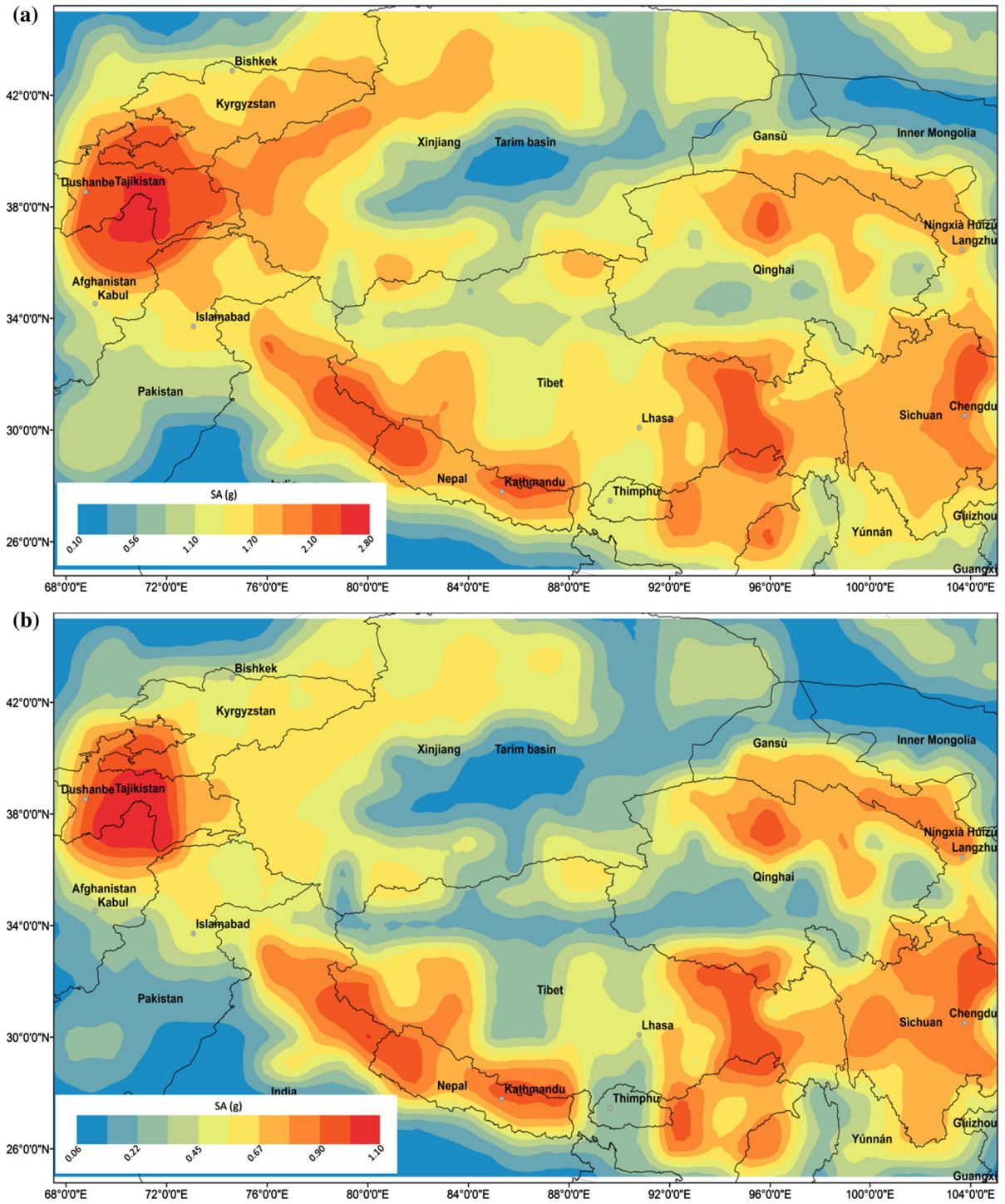

Figure 5
Hazard maps of spectral acceleration at **a** 0.2 s natural period and **b** 1.0 s natural period for 2% probability of exceedance in 50 years

Hazard distribution pattern for Tien Shan region nearly agrees with that of the ground motion parameter zonation map of China (Gao 2003). The highest hazard value for this region is in the order of 0.60–0.67 g and is supported by the very active crustal deformation with high rate of seismicity, which is also evident from the historical and instrumental earthquake records (Gao 2003; Kaban and Yuanda 2014). Because of very low rate of seismicity and rigidness of the crust, the Tarim basin and Inner Mongolia is clearly identified as a low seismic hazardous region whereas the hazard value down as low as 0.04 g. The interior of the Tibetan plateau excluding the isolated zone near to Lhasa is likely to be exposed in medium-to-low hazard value, whereas medium-to-high hazard is found at the plateau flank, particularly in the northwest plateau and in the eastern Himalayan syntaxis.

Predicted seismic hazard value increases significantly with decreasing the probability of exceedance. For example, at 2% probability of exceedance in 50 years, the expected level of hazard value is found to be a factor of 2 higher than that of 10% probability of exceedance in 50 years (Fig. 4b). In Fig. 4b, the estimates of minimum and maximum PGA values are observed as 0.07 and 1.50 g, respectively. The seismic hazard maps for SA values (Fig. 5a, b), which are produced as per the requirement of the modern building design provisions, show fairly similar distribution patterns as that of PGA hazard maps. The levels of SA value at 0.2 and 1.0 s natural periods for 2% probability of exceedance in 50 years are obtained in the order of 0.10–2.80 g and 0.06–1.10 g, respectively.

For making comparison, we also conducted PSHA using the short duration earthquake catalog since 1960 and estimating the Gutenberg–Richter parameter b value by the method of Aki (1965). Figure 6a shows the illustration of PGA value for 10% probability of exceedance from earthquake catalog since 1960. It is observed from the comparison (Figs. 4a, 6a) that the newly developed method of Kijko et al. (2016) which accounts the wide span of earthquake history (i.e., incomplete historical earthquakes records and complete instrumental seismic-event catalogs); uncertainties of the rate of seismicity, b value and M_{max} provide better results in terms of both hazard level and its spatial distribution. In Fig. 4a, the maximum hazard value is up to 0.87 g, which is about 32% higher than that of 0.67 g, as shown in Fig. 6a. The result obtained by applying the new approach is comparatively higher and rather flat than that of current seismic hazard maps for this region (e.g., Fig. 6b, c).

The hazard maps of this analysis show high values at some regions, where current existing hazard maps showed very low value. For example, near the location of 12 May 2008, M_w 7.9 Wenchuan earthquake, the ground motion parameter is significantly underestimated in the China ground motion zoning map (Liu et al. 2013) and most of the area is placed in zone II with very low zoning factor of as high as 0.15 g (Gao 2003; Fig. 6c). From Fig. 4a, we can find that at the location of the Wenchuan earthquake, the resulting hazard value of this analysis is higher (>0.43 g) than that predicted by China seismic zoning hazard maps (Fig. 6c), but consistent with the result of Liu et al. (2013) who used the historical intensity catalog. In the context of regional seismic hazard maps, the level of maximum seismic hazard value for 10% probability of exceedance in this analysis is found to be increased by $\sim$70 and 52% in Pamir–Hindu Kush region, and 34 and 20% in central Himalayan region from the results of Bhatia et al. (1999) and Zhang et al. (1999), respectively.

In addition, another comparison is made to illustrate the effect of different source models to the predicted hazard value. For convenience, a small part of the study area (Nepal) is considered, and illustrated on the basis of the result obtained using the conventional PSHA method. It seems that the contribution of different source models to the seismic hazard value is not same at every point and thereby varied spatially and temporarily. The deviation of hazard value with respect to the various source models is described by computing the seismic hazard curves for different cities of Nepal (Fig. 7). In the southern and central-western Nepal (e.g., nearby the cities of Bara, and Rukum), linear source contributes much higher seismic hazards than those of other two source models and consequently augments the levels of combined hazard value. For the central portion of Nepal around the Kathmandu city, the contribution is quite similar for all the models. In the southwest

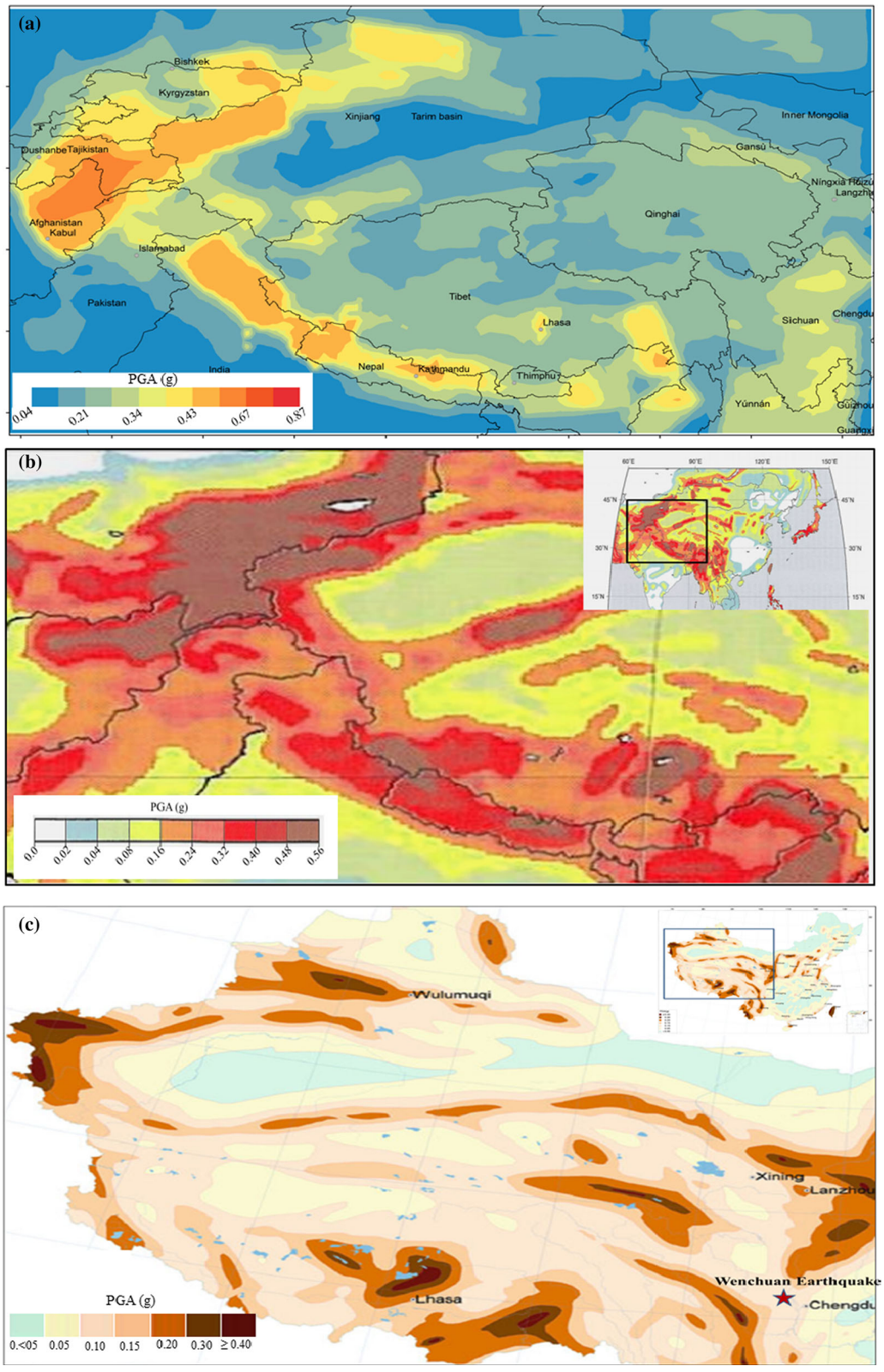

◀Figure 6
PGA hazard maps for 10% probability of exceedance in 50 years: **a** in this study computed from instrumental earthquake catalog; **b** Global Seismic Hazard Assessment Program (Zhang et al. 1999); and **c** Seismic Ground Motion Parameter Zonation Map of China (GB 18306-2001 2001)

region (near Kailali city), the highest contribution is from smoothed-gridded seismicity. Besides, the level of maximum hazard value is found to be as high as 0.54, 0.58, and 0.66 g for areal, linear, and smoothed-gridded source models, respectively, for 10%

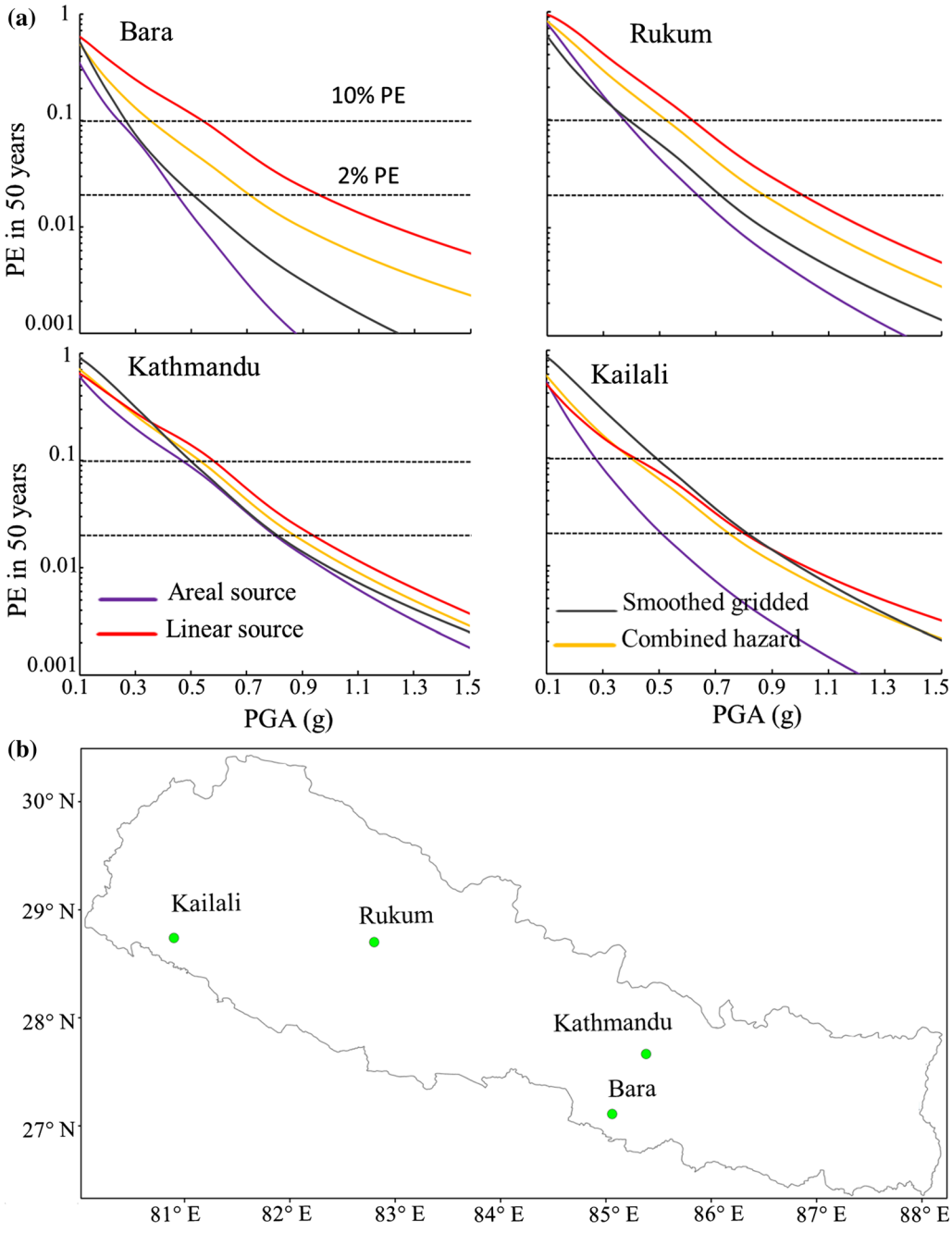

Figure 7
a Seismic hazard (PGA) curves for different cites of Nepal; **b** location map of these cities

probability of exceedance. It is noted that the hazard values for areal source model are nearly similar to the previous hazard maps of Nepal, while the maximum values are in the order of 0.50–0.54, 0.52–0.62, 0.45–0.50, and 0.48–0.56 g for this study, shown by Ram and Wang (2013), Chaulagain et al. (2015), and Zhang et al. (1999), respectively. However, the combined hazard value in this case is reasonably higher than that of the value for traditional areal source model and consistent with the results of similar seismogenic source models in India (e.g., Kolathayar and Sitharam 2012; Nath and Thingbaijam 2012). The incorporation of the past seismicity data (e.g., historical catalog and paleoseismic results) and instrumental catalog in the combination of multiple source models provides more comprehensive and explainable constraints to the predicted values of the ground motions.

4. Conclusion

We incorporated the latest data sets, multiple seismogenic source considerations, updated GMPEs, well-constrained focal depth, and newly developed methodology (Kijko et al. 2016) for the estimate of seismicity parameters for Himalayan–Tibetan region. All the uncertainties associated with the essential seismicity parameters (e.g., β, γ, and M_{max}) and the epistemic uncertainties of different models are taken into account. An unified declustered instrumental earthquake catalog and historical earthquake catalog since the tenth century are utilized in this hazard assessment. A total of 63 areal source zones, 228 active linear sources, and thousands of smoothed-gridded sources are identified and employed using a logic tree structure. The seismicity parameters for each of the seismic belts and areal source zones are computed by taking into account the incompleteness of the catalog, the uncertainty in the earthquake magnitude determination, as well as the uncertainty associated with the applied earthquake-occurrence models. To get more precise estimates of the earthquake parameters, different sub-sets of the catalog with different levels of completeness are assessed. The modified Gutenberg–Richter and Characteristic-earthquake magnitude–frequency models and two sets of GMPEs (four GMPEs for the active shallow crust and four GMPEs for the subduction interface) are used.

The hazard distribution is computed in terms of PGA for 10 and 2% probabilities of exceedance on bedrock level in 50 years. The spectral acceleration distribution maps at short and long natural periods (i.e., 0.2 and 1.0 s) are also produced for 2% probability of exceedance. To illustrate the resulting hazard value, two different comparisons are made: one is between the results from the newly adopted and conventional methods; and the other is between the inter-seismogenic source models. The present result depicts that the level of hazard value is rather higher than that of the previous hazard maps. The region of low background seismicity shows relatively higher value than the previous studies. The resulting hazard maps would provide new insights in improving the national building design provisions for Himalayan–Tibetan region. For better constraints of seismogenic sources, detail paleoseismic and geodetic studies are necessary. Strong ground motion records are essential in developing attenuation equations to make a better choice of GMPEs for this complex tectonic regime.

Acknowledgements

This research was supported by the grant of the National Nature Science Foundation of China (No. 41490611) to L.B., and by the President's PhD Fellowship of the Chinese Academy of Sciences (CAS) and The World Academy of Sciences (TWAS) to M.M.R. We used earthquake catalogs from the ISC, USGS, GEM, CSN, NOAA, and NSC. We are grateful to the guest editor Zhigang Peng and two anonymous reviewers for their constructive comments and thoroughly review on the manuscript. We thank Fabrice Cotton for the useful discussions. We are grateful to Andrzej Kijko and his colleagues for providing the "HA3" program and Mario Ordaz for providing the recently developed version of the CRISIS software.

References

Abrahamson, N., Gregor, N., & Addo, K. (2016). BC hydro ground motion prediction equations for subduction earthquakes. *Earthquake Spectra, 32*(1), 23–44. doi:10.1193/051712EQS188MR.

Abrahamson, N. A., Silva, W. J., & Kamai, R. (2014). Summary of the ASK14 ground motion relation for active crustal regions. *Earthquake Spectra, 30*(3), 1025–1055.

Ader, T., Avouac, J. P., Liu-Zeng, J., Lyon-Caen, H., Bollinger, L., Galetzka, J., et al. (2012). Convergence rate across the Nepal Himalaya and interseismic coupling on the Main Himalayan Thrust: Implications for seismic hazard. *Journal of Geophysical Research: Solid Earth, 117*(4), 1–16.

Aki, K. (1965). Maximum likelihood estimate of b in the formula log (N) = a − bM and its confidence limits. *Bulletin of the Earthquake Research Institute, University of Tokyo, 43,* 237–239.

Ambraseys, N. N., & Douglas, J. (2004). Magnitude calibration of north Indian earthquakes. *Geophysical Journal International, 159*(1), 165–206.

Ambraseys, N. N., Douglas, J., Sarma, S. K., & Smit, P. M. (2005). Equations for the estimation of strong ground motions from shallow crustal earthquakes using data from Europe and the Middle East: Horizontal peak ground acceleration and spectral acceleration. *Bulletin of Earthquake Engineering, 3*(1), 1–53.

Atkinson, G. M., & Boore, D. M. (2003). Empirical ground-motion relations for subduction-zone earthquakes and their application to Cascadia and other regions. *Bulletin of the Seismological Society of America, 93*(4), 703–1729.

Avouac, J.-P., Meng, L., Wei, S., Wang, T., & Ampuero, J.-P. (2015). Lower edge of locked Main Himalayan Thrust unzipped by the 2015 Gorkha earthquake. *Nature Geoscience, 8*(9), 708–711.

Avouac, J.-P., & Tapponnier, P. (1993). Kinematic model of active deformation in central Asia. *Geophysical Research Letters, 20*(10), 895–898. doi:10.1029/93GL00128.

Bai, L., Li, G., Khan, N. G., Zhao, J., & Ding, L. (2017). Focal depths and mechanisms of shallow earthquakes in the Himalayan–Tibetan region. *Gondwana Research, 41,* 390–399.

Bai, L., Liu, H., Ritsema, J., Mori, J., Zhang, T., Ishikawa, Y., et al. (2016). Faulting structure above the Main Himalayan Thrust as shown by relocated aftershocks of the 2015 M_w 7.8 Gorkha, Nepal, earthquake. *Geophysical Research Letters, 43*(2), 637–642.

Bai, L., Ritsema, J., & Zhao, J. (2012). Focal depth estimates of earthquakes in the Himalayan–Tibetan region from teleseismic waveform modeling. *Earthquake Science, 25*(5–6), 459–468.

Bai, L., & Zhang, T. (2015). Complex deformation pattern of the Pamir-Hindu Kush region inferred from multi-scale double-difference earthquake relocations. *Tectonophysics, 638*(1), 177–184. doi:10.1016/j.tecto.2014.11.006.

Benjamin, J. R. (1968). Probabilistic models for seismic forces design. *Journal of the Structural Division, 94*(5), 1175–1196.

Berryman, K., Ries, W., & Litchfield, N. (2014). The Himalayan frontal thrust: Attributes for seismic hazard Version 1.0, GEM Faulted Earth Project, available from http://www.nexus.globalquakemodel.org/. Accessed 10 Apr 2017.

Bhatia, S. C., Kumar, M. R., & Gupta, H. K. (1999). A probabilistic seismic hazard map of India and adjoining regions. *Annali di Geofisica, 42*(6), 1153–1164.

Bilham, R. (2013). Societal and observational problems in earthquake risk assessments and their delivery to those most at risk. *Tectonophysics, 584,* 166–173. doi:10.1016/j.tecto.2012.03.023.

Bilham, R. (2015). Raising Kathmandu. *Nature Geoscience, 8*(8), 582–584.

Bollinger, L., Tapponnier, P., Sapkota, S. N., & Klinger, Y. (2016). Slip deficit in central Nepal: Omen for a pending repeat of the 1344 AD earthquake? *Earth, Planets and Space, 68,* 1–12. doi:10.1186/s40623-016-0389-1.

Bommer, J. J., Scherbaum, F., Bungum, H., Cotton, F., Sabetta, F., & Abrahamson, N. A. (2005). On the use of logic trees for ground-motion prediction equations in seismic-hazard analysis. *Bulletin of the Seismological Society of America, 95*(2), 377–389.

Chaulagain, H., Rodrigues, H., Silva, V., Spacone, E., & Varum, H. (2015). Seismic risk assessment and hazard mapping in Nepal. *Natural Hazards, 78*(1), 583–602. doi:10.1007/s11069-015-1734-6.

Chiou, B. S. J., & Youngs, R. R. (2014). Update of the Chiou and Youngs NGA model for the average horizontal component of peak ground motion and response spectra. *Earthquake Spectra, 30*(3), 1117–1153.

Cornell, C. A. (1968). Engineering seismic risk analysis. *Bulletin of the Seismological Society of America, 58*(5), 1583–1606.

Cornell, C. A, & Van Marke, E. H. (1969). The major influences on seismic risk. In: Proceedings of the third world conference on earthquake engineering, Santiago, Chile, A-1; 69–93.

Cotton, F., Scherbaum, F., Bommer, J. J., & Bungum, H. (2006). Criteria for selecting and adjusting ground-motion models for specific target regions: Application to central Europe and rock sites. *Journal of Seismology, 10*(2), 137–156. doi:10.1007/s10950-005-9006-7.

Danciu, L., Pagani, M., Monelli, D., & Wiemer, S. (2010). *GEM1 Hazard: Overview of PSHA Software, GEM Technical Report 2010–2012*. Pavia: GEM Foundation.

Frankel, A. (1995). Mapping seismic hazard in the central and Eastern United States. *Seismological Research Letters, 66*(4), 8–21.

Gao, M. (2003). New national seismic zoning map of China. *Acta Seismologica Sinica, 16*(6), 639–645. doi:10.1007/s11589-003-0048-z.

Gardner, J., & Knopoff, L. (1974). Is the sequence of earthquakes in southern California, with aftershocks removed, Poissonian. *Bulletin of the Seismological Society of America, 64*(5), 1363–1367.

GB 18306-2001 (2001). Seismic Ground Motion Parameter Zonation Map of China. Standard Press, Beijing.

Grünthal, G., & Wahlström, R. (2003). An earthquake catalogue for central, northern and northwestern Europe based on M_w magnitudes. *Journal of Seismology, 7*(4), 507–531. doi:10.1023/B:JOSE.0000005715.87363.13.

Hanks, T. C., & Kanamori, H. (1979). A moment magnitude scale. *Journal of Geophysical Research: Solid Earth, 84*(B5), 2348–2350.

Kaban, M. K., & Yuanda, T. R. (2014). Density structure, isostatic balance and tectonic models of the Central Tien Shan. *Surveys in Geophysics, 35*(6), 1375–1391. doi:10.1007/s10712-014-9298-7.

Kaviris, G., Papadimitriou, P., Chamilothoris, L., & Makropoulos, K. (2008). Moment magnitudes for small and intermediate earthquakes. In *31 General Assembly of the European Seismological Commission,* Sept 7–12, 2008.

Khan, N., Bai, L., Junmeng, Z., Li, G., Rahman, M. M., Cheng, C., et al. (2017). Crustal structure beneath Tien Shan orogenic belt and its adjacent regions found by multi-scale seismic data. *Science China Earth Sciences*. doi:10.1007/s11430-017-9068-0.

Kijko, A., & Singh, M. (2011). Statistical tools for maximum possible earthquake magnitude estimation. *Acta Geophysica, 59*(4), 674–700.

Kijko, A., & Smit, A. (2012). Extension of the Aki-Utsu b-value estimator for incomplete catalogs. *Bulletin of the Seismological Society of America, 102*(3), 1283–1287. doi:10.1785/0120110226.

Kijko, A., Smit, A., & Sellevoll, M. A. (2016). Estimation of earthquake hazard parameters from incomplete data files. Part III. Incorporation of uncertainty of earthquake-occurrence model. *Bulletin of the Seismological Society of America*. doi:10.1785/0120150252.

Kolathayar, S., & Sitharam, T. G. (2012). Comprehensive probabilistic seismic hazard analysis of the Andaman-Nicobar regions. *Bulletin of the Seismological Society of America, 102*(5), 2063–2076. doi:10.1785/0120110219.

Lee, W. H. K., Wu, F. T., & Jacobsen, C. (1976). A catalog of historical earthquakes in China complied from recent Chinese publications. *Bulletin of the Seismological Society of America, 66*(6), 2003–2016.

Liu, J., Wang, Z., Xie, F., & Lv, Y. (2013). Seismic hazard assessment for greater North China from historical intensity observations. *Engineering Geology, 164,* 117–130.

Nath, S. K., & Thingbaijam, K. K. S. (2012). Probabilistic seismic hazard assessment of India. *Seismological Research Letters, 83*(1), 135–149.

Ordaz, M. G., Cardona, O.-D., Salgado-Gálvez, M. A., Bernal-Granados, G. A., Singh, S. K., & Zuloaga-Romero, D. (2014). Probabilistic seismic hazard assessment at global level. *International Journal of Disaster Risk Reduction, 10,* 419–427.

Ordaz, M., Faccioli, E., Martinelli, F., Aguilar, A., Arboleda, J., Meletti, C., & D'Amico, V. (2015). CRISIS2015 version 2.2: Computer program for computing seismic hazard. Instituto de Ingenieria, UNAM, Mexico.

Ornthammarath, T., Warnitchai, P., Worakanchana, K., Zaman, S., Sigbjörnsson, R., & Lai, C. G. (2011). Probabilistic seismic hazard assessment for Thailand. *Bulletin of Earthquake Engineering, 9*(2), 367–394.

Pandey, M. R., Chitrakar, G. R., Kafle, B., Sapkota, S. N., Rajaure, S. N., & Gautam, U. P. (2002). *Seismic hazard map of Nepal*. Kathmandu: Department of Mines and Geology.

Pandey, M. R., Tandukar, R. P., Avouac, J. P., Vergne, J., & Héritier, T. (1999). Seismotectonics of the Nepal Himalaya from a local seismic network. *Journal of Asian Earth Sciences, 17*(5–6), 703–712.

Priestley, K., James, J., & Mckenzie, D. (2008). Lithospheric structure and deep earthquakes beneath India, the Himalaya and southern Tibet. *Geophysical Journal International, 172*(1), 345–362.

Rajendran, C. P., John, B., & Rajendran, K. (2015). Medieval pulse of great earthquakes in the central Himalaya: Viewing past activities on the frontal thrust. *Journal of Geophysical Research: Solid Earth, 120*(3), 1623–1641. doi:10.1002/2014JB011015.

Ram, T. D., & Wang, G. (2013). Probabilistic seismic hazard analysis in Nepal. *Earthquake Engineering and Engineering Vibration, 12*(4), 577–586. doi:10.1007/s11803-013-0191-z.

Sabetta, F., Lucantoni, A., Bungum, H., & Bommer, J. J. (2005). Sensitivity of PSHA results to ground motion prediction relations and logic-tree weights. *Soil Dynamics and Earthquake Engineering, 25*(4), 317–329.

Sapkota, S. N., Bollinger, L., Klinger, Y., Tapponnier, P., Gaudemer, Y., & Tiwari, D. (2013). Primary surface ruptures of the great Himalayan earthquakes in 1934 and 1255. *Nature Geoscience, 6*(1), 71–76. doi:10.1038/ngeo1669.

Sawires, R., Peláez, J. A., Fat-Helbary, R. E., & Ibrahim, H. A. (2016). Updated probabilistic seismic hazard values for Egypt. *Bulletin of the Seismological Society of America, 106,* 1788–1801.

Scordilis, E. M. (2006). Empirical global relations converting MS and mb to moment magnitude. *Journal of Seismology, 10*(2), 225–236.

Sloan, R. A., Jackson, J. A., Mckenzie, D., & Priestley, K. (2011). Earthquake depth distributions in central Asia, and their relations with lithosphere thickness, shortening and extension. *Geophysical Journal International, 185*(1), 1–29. doi:10.1111/j.1365-246X.2010.04882.x.

Stepp, J. C. (1972). Analysis of completeness of the earthquake sample in the Puget Sound area and its effect on statistical estimates of earthquake hazard. *Proceedings of the 1st International Conference on Microzonazion, Seattle* (Vol. 2, pp. 897–910).

Stewart, J. P., Douglas, J., Javanbarg, M. B., Alessandro, C. Di, Bozorgnia, Y., Abrahamson, N. A., & Stafford, P. J. (2013). GEM-PEER Task 3 Project: Selection of a Global Set of Ground Motion Prediction Equations. PEER Report 2013/22; Available at www.nexus.globalquakemodel.org/. Accessed 10 Jan 2017.

Stirling, M., & Goded, T. (2012). Magnitude scaling relationships. *Report Produced for the GEM Faulted Earth & Regionalisation Global Components, GNS Science Miscellaneous Series, 42,* 35.

Styron, R., Taylor, M., & Okoronkwo, K. (2010). Database of active structures from the Indo-Asian Collision. *Eos (Washington. DC), 91*(20), 181–182. doi:10.1029/2010EO200001.

Szeliga, W., Hough, S., Martin, S., & Bilham, R. (2010). Intensity, magnitude, location, and attenuation in India for felt earthquakes since 1762. *Bulletin of the Seismological Society of America, 100*(2), 570–584.

Tapponnier, P., Xu, Z. Q., Roger, F., Meyer, B., Arnaud, N., Wittlinger, G., et al. (2001). Oblique stepwise rise and growth of the Tibet plateau. *Science, 294*(5547), 1671–1677. doi:10.1126/science.105978.

Tinti, S., & Mulargia, F. (1985). An improved method for the analysis of the completeness of a seismic catalogue. *Lett Al Nuovo Cimento, 42*(1), 7–21.

Wang, Z., Butler, D. T., Woolery, E. W., & Wang, L. (2012). Seismic hazard assessment for the Tianshui urban area, Gansu Province. *China. International Journal of Geophysics*. doi:10.1155/2012/461863.

Wells, D. L., & Coppersmith, K. J. (1994). New empirical relationships among magnitude, rupture length, rupture width, rupture area, and surface displacement. *Bulletin of the Seismological Society of America, 84*(4), 974–1002.

Wiemer, S., & Wyss, M. (2000). Minimum magnitude of completeness in earthquake catalogs: Examples from Alaska, the Western United States, and Japan. *Bulletin of the Seismological Society of America, 90*(4), 859–869. doi:10.1785/0119990114.

Woo, G. (1996). Kernel estimation methods for seismic hazard area source modelling. *Bulletin of the Seismological Society of America, 88,* 353–362.

Yen, Y. T., & Ma, K. F. (2011). Source-Scaling relationship for M 4.6–8.9 earthquakes, specifically for earthquakes in the Collision

Zone of Taiwan. *Bulletin of the Seismological Society of America, 101*(2), 464–481. doi:10.1785/0120100046.

Youngs, R. R., Chiou, S.-J., Silva, W. J., & Humphrey, J. R. (1997). Strong ground motion attenuation relationships for subduction zone earthquakes. *Seismological Research Letters, 68*(1), 58–73.

Zhang, P., Yang, Z., Gupta, H. K., Bhatia, S. C., & Shedlock, K. M. (1999). Global seismic hazard assessment program (GSHAP) in continental Asia. *Annali di Geofisica, 42*(6), 1167–1190. doi:10.4401/ag-3778.

Zhangming, W. (1992). Distribution of seismicity and active faults in Tibetan plateau. *Journal of Seismological Research, 15*(2), 210–218.

Zhao, J., Lu, F., Li, Z., Wang, Y., Ma, W., & Liu, X. (2012). Lithospheric structure and geodynamics at the northern margin of Tibetan plateau. *Earthquake Science, 25*(5), 433–450. doi:10.1007/s11589-012-0868-9.

Zhao, J. X., Zhang, J., Asano, A., Ohno, Y., Oouchi, T., Takahashi, T., et al. (2006). Attenuation relations of strong ground motion in Japan using site classification based on predominant period. *Bulletin of the Seismological Society of America, 96*(3), 898–913.

(Received June 11, 2017, revised August 17, 2017, accepted August 29, 2017, Published online September 11, 2017)